Applied Physics Letters

Phonon transport properties of two-dimensional electride Ca_2N—A first-principles study

Cite as: Appl. Phys. Lett. **113**, 131902 (2018); https://doi.org/10.1063/1.5051465
Submitted: 08 August 2018 . Accepted: 10 September 2018 . Published Online: 28 September 2018

Matthew C. Barry, Zhequan Yan, Mina Yoon, Surya R. Kalidindi, and Satish Kumar

Phonon transport properties of two-dimensional electride Ca_2N—A first-principles study

Matthew C. Barry,[1] Zhequan Yan,[1] Mina Yoon,[2,a)] Surya R. Kalidindi,[1] and Satish Kumar[1,a)]
[1]*G.W. Woodruff School of Mechanical Engineering, Georgia Institute of Technology, Atlanta, Georgia 30332, USA*
[2]*Center for Nanophase Materials Sciences, Oak Ridge National Laboratory, Oak Ridge, Tennessee 37831, USA*

(Received 8 August 2018; accepted 10 September 2018; published online 28 September 2018)

We investigate phonon transport in dicalcium nitride (Ca_2N), an electride with two-dimensional confined electron layers, using first-principles density functional theory and the phonon Boltzmann transport equation. The in-plane ($\kappa_{[100]}$) and out-of-plane ($\kappa_{[001]}$) lattice thermal conductivities at 300 K are found to be 11.72 W m^{-1} K^{-1} and 2.50 W m^{-1} K^{-1}, respectively. Spectral analysis of lattice thermal conductivity shows that ~85% of $\kappa_{[100]}$ and $\kappa_{[001]}$ is accumulated by phonons with frequencies less than 5.5 THz and 2.5 THz, respectively. Modal decomposition of lattice thermal conductivity further reveals that the optical phonons contribute to ~68% and ~55% of overall $\kappa_{[100]}$ and $\kappa_{[001]}$, respectively. Phonon dispersion suggests that the large optical phonon contribution is a result of low frequency optical phonons with high group velocities and the lack of phonon bandgap between the acoustic and optical phonon branches. We find that the optical phonons with frequencies below ~5.5 THz have similar three-phonon phase space and scattering rates as acoustic phonons. Comparison of the contributions from emission and absorption processes reveals that the three-phonon phase space and scattering rates of phonons—optical or acoustic—with frequencies below 5.5 THz are largely dominated by absorption processes. We conclude that the large contribution to lattice thermal conductivity by optical phonons is due to the presence of multiple low frequency optical phonon modes with high group velocities and similar phase space and scattering rates as the acoustic phonons. This study provides the frequency and temperature dependent lattice thermal conductivity and insights into phonon transport in Ca_2N, both of which have important implications for the development of Ca_2N based devices. *Published by AIP Publishing.*
https://doi.org/10.1063/1.5051465

The electride dicalcium nitride (Ca_2N) has received significant attention for its potential applications in areas such as high-performance electronic devices[1] and chemical synthesis.[2] Ca_2N has a layered structure in which two-dimensional (2D) confined electrons behave as anions, a topology unique to 2D electride materials.[3–5] The existence of the free-electron-like electron layers of Ca_2N results in excellent electronic properties such as a low work function, a long electron mean free path, and a high electron mobility.[5] Additionally, it has been demonstrated theoretically that the Ca_2N structure has potential application as an effective electron transport channel due to the reduced nuclear scattering in its intrinsic two-dimensional electron gas in free space (2DEG-FS) state.[6] Ca_2N has been identified as a promising electronic device material, and it is important to study the thermal properties which can affect the electronic transport in devices using Ca_2N and remain unexplored.

In this letter, we use first-principles density functional theory (DFT) with the Boltzmann transport equation (BTE) to investigate the phonon transport properties and lattice thermal conductivity of Ca_2N. DFT calculations are performed using the Vienna *ab initio* simulation package (VASP).[7,8] A plane-wave basis set and the projector augmented-wave (PAW) method are used with the Perdew-Burke-Ernzerhof (PBE) generalized gradient approximation (GGA) exchange-correlation functional.[9–11] The Ca_2N hexagonal unit cell structure is optimized using a plane-wave basis cutoff energy of 700 eV and a $31 \times 31 \times 5$ Γ-centered grid of k-points for integration over the Brillouin zone. The convergence criteria for the energy and force are 10^{-9} eV and 10^{-5} eV/Å, respectively. The obtained lattice parameters, $a = 3.609$ Å and $c = 19.246$ Å, are within −0.56% and +0.60% of recent experimental results, respectively.[5] The second-order harmonic and third-order anharmonic interatomic force constants (IFCs) are calculated using $5 \times 5 \times 1$ and $3 \times 3 \times 1$ supercells, respectively, with a $3 \times 3 \times 3$ Γ-centered grid of k-points. The convergence criteria and plane-wave basis cutoff energy for IFC calculations are maintained at 10^{-9} eV and 700 eV, respectively. To properly account for interactions between atoms in neighboring layers, a large cutoff of 1 nm is used for computing the anharmonic IFCs using a finite displacement method.[12] This is sufficiently large to consider interactions between all atoms in a given pair of neighboring layers within a hexagonal unit cell. The dielectric tensor and Born effective charges are calculated from density functional perturbation theory and included in the phonon calculations to account for the longitudinal and transverse optical phonon (LO-TO) splitting at the Γ point. The phonon relaxation times and lattice thermal conductivity are

a)Authors to whom correspondence should be addressed: myoon@ornl.gov and satish.kumar@me.gatech.edu

calculated using Fermi's golden rule[13] with the iterative solution to the BTE.[14–16] A 19 × 19 × 5 mesh of q-points is used for the thermal conductivity calculations.

The electron band structure of the conventional hexagonal unit cell is shown in Fig. 1(a). The three bands cross the Fermi level with high dispersion along the $\Gamma \rightarrow M$ and $\Gamma \rightarrow K$ paths inside the Brillouin zone, which correspond to [100] and [110] in the real space hexagonal unit cell structure [Figs. 1(b) and 1(c)]. From $\Gamma \rightarrow A$ (along [001]), none of the bands cross the Fermi level, suggesting that electrons near the Fermi level may be two-dimensionally confined.[17] Previous studies show that the electrical conduction of Ca_2N and the bands crossing the Fermi level are related to the 2D confined anionic electron layers [represented by blue in Fig. 1(c)].[17–19] Our electron band structure is in good agreement with the current literature,[5,17] which uses computational methods similar to those used in this work. Features of our electronic structure, such as band dispersion widths, the maximum energy of the three bands that cross the Fermi level (∼1.25 eV), and the lack of bands crossing the Fermi level along the [001] direction, are also similar to those observed in earlier studies using different computational methods such as ultrasoft pseudopotentials, the localized spherical wave method, and the linear muffin-tin orbital method.[19,20] In conventional layered 2D materials, van der Waals (vdW) interactions are often needed to describe interlayer interactions. However, in 2D electrides, the anionic electrons distributed in the cavity space create a strong interlayer electrostatic interaction.[21] The Coulomb interaction becomes the critical component in stabilizing the electride layers, and the effect of vdW forces is negligible.[21,22] We confirmed that the interlayer distance of Ca_2N is accurately described without adding any vdW corrections. Our hexagonal lattice parameters, calculated without vdW corrections, are within −0.56% and +0.60% of recent experimental results[5] for *a* and *c*, respectively, whereas those including vdW corrections are within −0.94% and −1.25%, respectively.[1]

The phonon dispersion and projected density of states (PDOS) are shown in Figs. 1(d) and 1(e), respectively. We observe that heavier elements mostly contribute to the low frequency phonon modes—over 85% of the phonon DOS below 8.0 THz is from Ca atoms. All of the five significant peaks in the DOS (∼5.0 THz, ∼7.3 THz, ∼7.6 THz, ∼9.2 THz, and ∼13.5 THz) occur at frequencies common to multiple low group velocity phonon modes. The first peak (∼5.0 THz) is wide because there are many low group velocity phonon modes spanning the ∼4.5–5.5 THz range, whereas the fourth peak (∼9.2 THz) is narrow because the fewer low group velocity phonon modes contributing to the DOS are mostly degenerate. The thermal conductivity shows high directional anisotropy: our calculated in-plane ($\kappa_{[100]}$) and out-of-plane ($\kappa_{[001]}$) lattice thermal conductivities at 300 K are 11.72 W m^{-1} K^{-1} and 2.50 W m^{-1} K^{-1}, respectively. The temperature dependent lattice thermal conductivity also displays a strong directional anisotropy (Fig. 2). The in-plane thermal conductivity is ∼5X larger than the out-of-plane thermal conductivity at temperatures above 200 K and over 6.5X larger at 100 K. Fitting the thermal conductivity data to the function $k = AT^{-m}$ reveals that m is larger for $\kappa_{[100]}$ than $\kappa_{[001]}$; this means that $\kappa_{[100]}$ is more sensitive to temperature than $\kappa_{[001]}$ and suggests that Umklapp scattering is more dominant on $\kappa_{[100]}$ than on $\kappa_{[001]}$. The anisotropy of thermal conductivity and weaker temperature dependence of $\kappa_{[001]}$ are typical properties of layered materials.[23] The thermal conductivity of Ca_2N is significantly lower than that of one-atom thick layers, such as multi-layered graphene[24] ($\kappa_{[100]}$ – ∼2275 W m^{-1} K^{-1}) and hexagonal boron nitride[25] ($\kappa_{[100]}$ – ∼445 W m^{-1} K^{-1}), while it is comparable to some of the multi-atom thick layered structures, such as MoS_2[26,27]

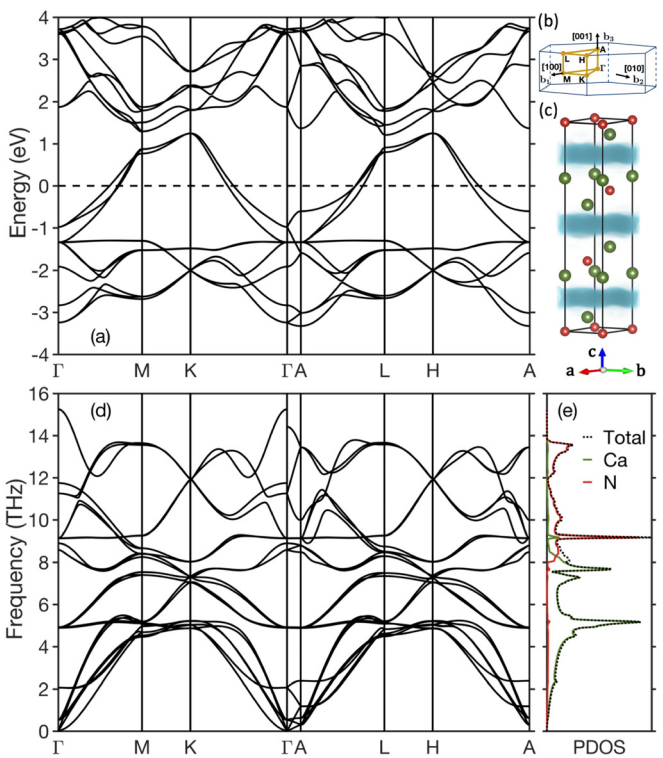

FIG. 1. (a) The electron band structure of Ca_2N along high symmetry paths in the first Brillouin zone of the conventional hexagonal unit cell. (b) The Brillouin zone of the conventional hexagonal unit cell.[33] (c) The hexagonal unit cell structure with calcium atoms given in green, nitrogen atoms given in red, and a representation of the electron layers given in blue. (d) The phonon dispersion along high symmetry points in the first Brillouin zone of the conventional hexagonal unit cell. (e) The phonon projected density of states.

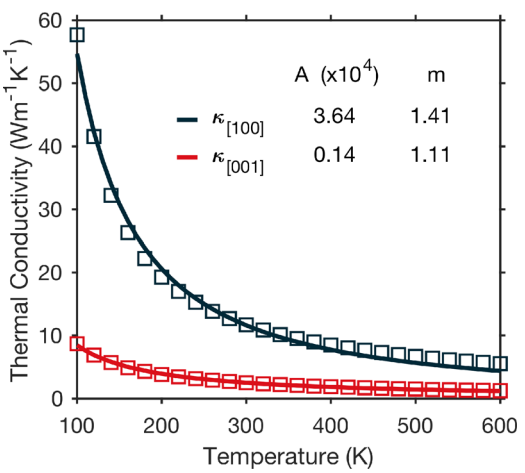

FIG. 2. Temperature dependent lattice thermal conductivity of Ca_2N. The squares are the calculated values, and the lines show a fit to the function $\kappa = AT^{-m}$.

(multi-layer $\kappa_{[100]} - 52\,\mathrm{W\,m^{-1}\,K^{-1}}$; bulk $\kappa_{[100]} - 110\,\mathrm{W\,m^{-1}\,K^{-1}}$), multi-layered phosphorene[28] (zigzag $- 5.57\,\mathrm{W\,m^{-1}\,K^{-1}}$; armchair $- 2.32\,\mathrm{W\,m^{-1}\,K^{-1}}$), and Bi_2Te_3[23] ($\kappa_{[100]} - 1.7\,\mathrm{W\,m^{-1}\,K^{-1}}$; $\kappa_{[001]} - 0.8\,\mathrm{W\,m^{-1}\,K^{-1}}$). The lower thermal conductivity of the multi-atom thick layered materials is due to large atomic masses and non-flat monolayer structures.

We further analyze the frequency dependent lattice thermal conductivity of each phonon mode. The first significant peak in the DOS [Fig. 1(e)] covers the ~4.5–5.5 THz range. The accumulated thermal conductivity at 300 K shows that over 85% of both $\kappa_{[100]}$ and $\kappa_{[001]}$ is accumulated by phonons with frequencies below the 5.5 THz upper limit of this peak (Fig. 3). Furthermore, over 75% of the total optical mode contribution to $\kappa_{[100]}$ and $\kappa_{[001]}$ is accumulated by optical phonons with frequencies below 5.5 THz. This result is supported by the phonon dispersion [Fig. 1(d)], which shows that Ca_2N has multiple low frequency optical phonon modes. From $\Gamma \rightarrow M$ (along [100]), these modes have a large group velocity and reach a maximum at a frequency of ~5.5 THz, whereas from $\Gamma \rightarrow A$ (along [001]), the major contributions to thermal conductivity are by the first transverse acoustic (TA1) mode and the optical modes below a frequency of 2.5 THz. The large TA1 contribution to $\kappa_{[001]}$ is explained by the high group velocity from $\Gamma \rightarrow A$ (along [001]).

Figure 3 shows that the optical phonon modes comprise a significant percentage of the total lattice thermal conductivity, contributing to over 68% and 55% of the total $\kappa_{[100]}$ and $\kappa_{[001]}$, respectively. Although it is often the case that optical phonon contributions to thermal conductivity are negligible, they have been found to play a large role in many complex materials.[29] Furthermore, this result is well supported by the phonon dispersion, which shows no frequency

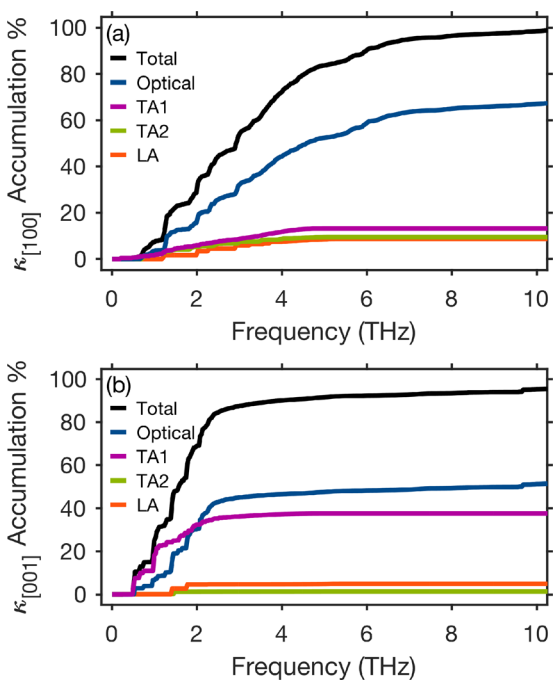

FIG. 3. Accumulation of (a) in-plane and (b) out-of-plane lattice thermal conductivities with phonon frequency. The individual phonon mode contributions to the total $\kappa_{[100]}$ and $\kappa_{[001]}$ from the first transverse acoustic (TA1), second transverse acoustic (TA2), longitudinal acoustic (LA), and optical phonon modes are shown.

bandgap between the acoustic and optical phonon branches, leading to higher probability of scattering for the acoustic modes. Additionally, the low frequency optical phonon modes have large group velocities similar in magnitude to those of the acoustic phonon modes.

To identify and understand the phonon transport mechanism responsible for the large optical mode thermal conductivity, we examine the three-phonon scattering phase space and phonon scattering rates (Fig. 4). The three-phonon scattering phase space indicates the percentage of allowed three-phonon processes and gives insight into the likelihood of phonon scattering. The total three-phonon scattering phase space is calculated as[30,31]

$$P_3 = \frac{2}{3n_j^3 V_{BZ}^2}\left(P_3^{(+)} + \frac{1}{2}P_3^{(-)}\right), \tag{1}$$

where V_{BZ} is the Brillouin zone volume and n_j is the number of phonon branches. $P_3^{(+)}$ and $P_3^{(-)}$ are the separate contributions to total phase space from the absorption and emission processes, respectively, and evaluated as

$$P_3^{(\pm)} = \sum_j \int d\boldsymbol{q} D_j^{(\pm)}(\boldsymbol{q}), \tag{2}$$

where

$$D_j^{(\pm)}(\boldsymbol{q}) = \sum_{j',j''} \int d\boldsymbol{q}' \delta\left(\omega_j(\boldsymbol{q}) \pm \omega_{j'}(\boldsymbol{q}') - \omega_{j''}(\boldsymbol{q}'')\right), \tag{3}$$

where $\mathbf{q}$ and j are the wave-vector and polarization of a phonon mode, respectively, and $\omega_j(\boldsymbol{q})$ is the phonon frequency of the mode $(j, \boldsymbol{q})$. The prime and double prime differentiate between phonon modes in a three-phonon scattering process satisfying both conservation of energy, $\omega_j(\boldsymbol{q}) \pm \omega_{j'}(\boldsymbol{q}') = \omega_{j''}(\boldsymbol{q}'')$, and momentum, $\boldsymbol{q} \pm \boldsymbol{q}' = \boldsymbol{q}'' + \mathbf{G}$, where $\mathbf{G}$ is a reciprocal lattice vector that is only non-zero for Umklapp processes. The three-phonon scattering rates are calculated as[32]

$$\Gamma^{\pm}_{\lambda\lambda'\lambda''} = \frac{\hbar\pi}{4N_0} \frac{\left|V^{\pm}_{\lambda,\lambda',\lambda''}\right|^2 \left(n^0_\lambda + 1\right)\left(n^0_{\lambda'} + 1/2 \pm 1/2\right) n^0_{\lambda''}}{\omega_\lambda \omega_{\lambda'} \omega_{\lambda''}} \times \delta(\omega_\lambda \pm \omega_{\lambda'} - \omega_{\lambda''}), \tag{4}$$

where n^0_λ is the Bose-Einstein distribution function for phonon angular frequency ω_λ and N_0 is the number of unit cells. $\Gamma^{+}_{\lambda\lambda'\lambda''}$ and $\Gamma^{-}_{\lambda\lambda'\lambda''}$ are the separate contributions to the three-phonon scattering rates from the absorption and emission processes, respectively. $V_{\lambda,\lambda',\lambda''}$ is the three-phonon scattering matrix given by

$$V_{\lambda,\lambda',\lambda''} = \sum_{0k}\sum_{l'k'}\sum_{l''k''}\sum_{\alpha\beta\gamma} \Phi_{\alpha\beta\gamma}(0k, l'k', l''k'') \times \frac{e^{\lambda}_{\alpha k} e^{\lambda'}_{\alpha k'} e^{\lambda''}_{\alpha k''}}{\sqrt{M_k M_{k'} M_{k''}}} e^{i\vec{q}'\cdot\vec{R}_{l'}} e^{i\vec{q}''\cdot\vec{R}_{l''}}, \tag{5}$$

where l and k specify the k^{th} atom in unit cell l and $e^{\lambda}_{\alpha k}$ is the α^{th} component of the phonon eigenvector for atom k of the unit cell in mode λ. $\vec{R}_l$ is the location of unit cell l and $\Phi_{\alpha\beta\gamma}(0k, l'k', l''k'')$ are the third-order anharmonic IFCs.

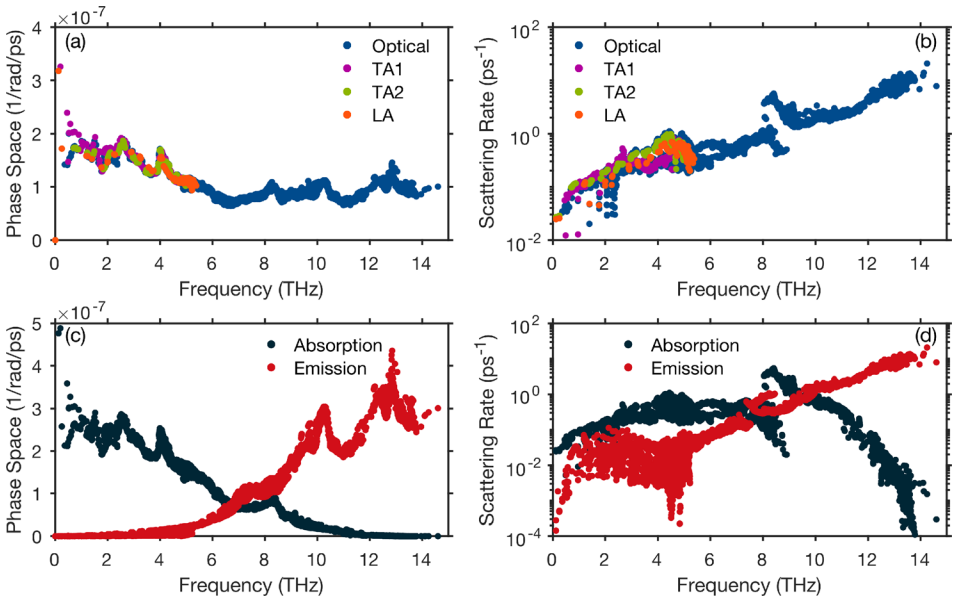

FIG. 4. The mode decomposed (a) three-phonon scattering phase space and (b) scattering rates. The separate absorption and emission contributions to (c) three-phonon scattering phase space and (d) scattering rates.

The phase space of optical phonons with frequencies below 5.5 THz is on average larger than that of optical phonons with frequencies above 5.5 THz [Fig. 4(a)]. Therefore, optical phonons with frequencies less than 5.5 THz have more available channels for phonon scattering processes than those with frequencies above 5.5 THz. The three-phonon phase space of optical phonons with frequencies below 5.5 THz is very similar to that of the acoustic phonons, and they also have similar phonon scattering rates [Fig. 4(b)]. As a result, it is reasonable to suspect that an acoustic and optical phonon with similar frequencies would have similar contributions to thermal conductivity. In this case, the multiple low frequency optical phonon modes would make a substantial contribution to the total thermal conductivity. Decomposition of the three-phonon scattering phase space and scattering rates into emission and absorption processes reveals that the phase space and scattering rates of phonons with frequencies below 5.5 THz are largely dominated by absorption processes [Figs. 4(c) and 4(d)]. This means that below 5.5 THz, there is a high probability of phonon scattering processes in which a lower energy phonon is converted into a higher energy phonon by absorbing a phonon. The three-phonon scattering phase space also shows five peaks over the complete phonon frequency range. The first two of these peaks (~2.6 THz and ~4.1 THz) appear in the absorption dominated spectrum, whereas the last two (~10.4 THz and ~12.9 THz) appear in the emission dominated spectrum. The middle peak (~8.3 THz) appears where both absorption and emission processes are important. This is also reflected in the phonon scattering rates; the low frequency peaks are correlated with high absorption scattering rates, whereas the high frequency peaks are correlated with high emission scattering rates. At the middle frequency peak, the absorption and emission scattering rates are very similar.

In conclusion, we calculate the lattice thermal conductivity in Ca_2N and investigate its phonon transport using first-principles methods and the phonon Boltzmann transport equation. We find that the in-plane and out-of-plane lattice thermal conductivities at 300 K are 11.72 W m^{-1} K^{-1} and 2.50 W m^{-1} K^{-1}, respectively. The phonon dispersion reveals that Ca_2N has multiple low frequency optical phonon modes with high group velocities and no frequency bandgap between the acoustic and optical phonon branches. Analysis of the frequency dependence of thermal conductivity shows that over 85% of the total $\kappa_{[100]}$ and $\kappa_{[001]}$ is accumulated by phonons with frequencies below 5.5 THz. The individual phonon mode contributions to thermal conductivity reveal that over 68% and 55% of the total $\kappa_{[100]}$ and $\kappa_{[001]}$ is contributed by optical phonons. Furthermore, over 75% of optical $\kappa_{[100]}$ and $\kappa_{[001]}$ is accumulated by optical phonons with frequencies below 5.5 THz. The three-phonon scattering phase space and scattering rates of acoustic phonons and optical phonons with frequencies less than 5.5 THz are very similar in magnitude, and both are dominated by absorption processes. We conclude that the large optical contribution to thermal conductivity in Ca_2N is due to multiple low frequency optical phonon modes with very similar phonon transport properties to those of the acoustic phonon modes. These results may have important implications for the development of Ca_2N based devices.

This work was supported in part by National Science Foundation Grant No. 1258425. Part of this research was performed at the Center for Nanophase Materials Sciences, which is a DOE Office of Science User Facility, supported by the U.S. Department of Energy, Office of Science, Basic Energy Sciences (BES), Materials Sciences and Engineering Division and by the Creative Materials Discovery Program through the National Research Foundation of Korea (NRF) funded by the Ministry of Science, ICT and Future Planning (No. NRF-2016M3D1A1919181). Computing resources were provided by the National Energy Research Scientific Computing Center, which was supported by the Office of Science of the U.S. Department of Energy under Contract No. DE-AC02-05CH11231.

[1]S. Guan, S. A. Yang, L. Zhu, J. Hu, and Y. Yao, Sci. Rep. **5**, 12285 (2015).
[2]D. L. Druffel, K. L. Kuntz, A. H. Woomer, F. M. Alcorn, J. Hu, C. L. Donley, and S. C. Warren, J. Am. Chem. Soc. **138**(49), 16089 (2016).
[3]J. L. Dye, Science **301**(5633), 607 (2003).

[4]J. L. Dye, Acc. Chem. Res. **42**(10), 1564 (2009).
[5]K. Lee, S. W. Kim, Y. Toda, S. Matsuishi, and H. Hosono, Nature **494**(7437), 336 (2013).
[6]S. Zhao, Z. Li, and J. Yang, J. Am. Chem. Soc. **136**(38), 13313 (2014).
[7]G. Kresse and J. Furthmüller, Comput. Mater. Sci. **6**(1), 15 (1996).
[8]G. Kresse and J. Furthmüller, Phys. Revi. B **54**(16), 11169 (1996).
[9]P. E. Blöchl, Phys. Rev. B **50**(24), 17953 (1994).
[10]G. Kresse and D. Joubert, Phys. Rev. B **59**(3), 1758 (1999).
[11]J. P. Perdew, K. Burke, and M. Ernzerhof, Phys. Rev. Lett. **77**(18), 3865 (1996).
[12]A. Togo and I. Tanaka, Scr. Mater. **108**, 1 (2015).
[13]A. A. Maradudin and A. E. Fein, Phys. Rev. **128**(6), 2589 (1962).
[14]W. Li, J. Carrete, N. A. Katcho, and N. Mingo, Comput. Phys. Commun. **185**(6), 1747 (2014).
[15]W. Li, N. Mingo, L. Lindsay, D. A. Broido, D. A. Stewart, and N. A. Katcho, Phys. Rev. B **85**(19), 195436 (2012).
[16]W. Li, L. Lindsay, D. A. Broido, D. A. Stewart, and N. Mingo, Phys. Rev. B **86**(17), 174307 (2012).
[17]T. Tada, S. Takemoto, S. Matsuishi, and H. Hosono, Inorg. Chem. **53**(19), 10347 (2014).
[18]A. Walsh and D. O. Scanlon, J. Mater. Chem. C **1**(22), 3525 (2013).
[19]C. M. Fang, G. A. de Wijs, R. A. de Groot, H. T. Hintzen, and G. de With, Chem. Mater. **12**(7), 1847 (2000).
[20]U. Steinbrenner, P. Adler, W. Hölle, and A. Simon, J. Phys. Chem. Solids **59**(9), 1527 (1998).
[21]W. Ming, M. Yoon, M.-H. Du, K. Lee, and S. W. Kim, J. Am. Chem. Soc. **138**(47), 15336 (2016).
[22]C. Park, S. W. Kim, and M. Yoon, Phys. Rev. Lett. **120**(2), 026401 (2018).
[23]B. Qiu and X. Ruan, Phys. Rev. B **80**(16), 165203 (2009).
[24]L. Lindsay, D. A. Broido, and N. Mingo, Phys. Rev. B **83**(23), 235428 (2011).
[25]L. Lindsay and D. A. Broido, Phys. Rev. B **85**(3), 035436 (2012).
[26]S. Sahoo, A. P. S. Gaur, M. Ahmadi, M. J.-F. Guinel, and R. S. Katiyar, J. Phys. Chem. C **117**(17), 9042 (2013).
[27]J. Liu, G.-M. Choi, and D. G. Cahill, J. Appl. Phys. **116**(23), 233107 (2014).
[28]Y.-Y. Zhang, Q.-X. Pei, J.-W. Jiang, N. Wei, and Y.-W. Zhang, Nanoscale **8**(1), 483 (2016).
[29]R. Guo, X. Wang, and B. Huang, Sci. Rep. **5**, 7806 (2015).
[30]L. Lindsay and D. A. Broido, J. Phys.: Condens. Matter **20**(16), 165209 (2008).
[31]Z. Yan, M. Yoon, and S. Kumar, 2D Mater. **5**(3), 031008 (2018).
[32]D. A. Broido, M. Malorny, G. Birner, N. Mingo, and D. A. Stewart, Appl. Phys. Lett. **91**(23), 231922 (2007).
[33]W. Setyawan and S. Curtarolo, Comput. Mater. Sci. **49**(2), 299 (2010).